Nuclear Instruments and Methods in Physics Research A 1093 (2027) 172078

Contents lists available at ScienceDirect

Nuclear Inst. and Methods in Physics Research, A

journal homepage: www.elsevier.com/locate/nima

Full Length Article

Stress minimization in DC-sputtered nickel thin films for optimized high-*m*-value Ni/Ti neutron supermirrors

Jose Manuel Gómez-Guzmán [a,*], Sabine Pütter [b]

[a] Heinz Maier-Leibnitz Zentrum, Technische Universität München, Lichtenbergstraße 1, Garching 85748, Germany
[b] Jülich Centre for Neutron Science (JCNS) at Heinz Maier-Leibnitz Zentrum (MLZ), Forschungszentrum Jülich GmbH, Lichtenbergstraße 1, Garching 85748, Germany

ARTICLE INFO

Keywords:
Neutron supermirrors
Residual stress
DC sputtering
Neutron reflectivity

ABSTRACT

Neutron supermirrors are multilayer structures of varying bilayer thickness and broadened Bragg-reflection range with the purpose of extending the coating's critical angle of total reflection, increasing the neutron flux reaching neutron instruments. Therefore, they are indispensable in many scattering and particle physics experiments. This study investigates the impact of synthetic air on the mechanical stress of nickel thin films and Ni/Ti neutron supermirrors prepared via reactive DC magnetron sputtering. Varying the fraction of synthetic air, X-ray Reflectivity (XRR) measurements on nickel thin films indicate an improvement of the surface roughness to 12 Å at an air-flow of 10 sccm to 12.5 sccm. X-ray Diffraction (XRD) measurements reveal crystallization of polycrystalline fcc-Ni phase for pure argon atmosphere and air-flows up to 3.5 sccm. At higher air-flows the fcc NiO phase coexists with polycrystalline and (020)-textured fcc Ni, and evolves with varying weight percentages. The stress developed in the thin film nickel samples during the DC sputtering process was determined by the XRD $\sin^2\psi$ and the wafer curvature method, and show similar behavior: it is compensated at about 10 sccm which coincides with the minimum grain size and surface roughness. Thanks to the optimized growth conditions, mechanically stable Ni/Ti supermirrors with high reflectivity and *m*-values up to $m = 5$, where *m* represents the number of times by which the critical angle of total reflection of the best reflecting material (nickel) is multiplied, are produced.

1. Introduction

Neutron supermirrors (SMs) consist of a stack of thin bilayers of slowly varying thickness so that at a given angle of incidence the Bragg condition is fulfilled for a wide range of the de Broglie wavelength of incident neutrons, or – for a given wavelength – the angular range of reflectivity close to unity is extended beyond the critical angle of total reflection of the best reflecting material, nickel, by a number of times, called the *m*-value of the SM [1]. By using neutron SMs, higher critical angles of reflection $\theta_{\mathrm{crit,SM}} = \theta_{\mathrm{crit,Ni}} \cdot \mathrm{m}$ can be achieved, where $\theta_{\mathrm{crit,Ni}} = 0.099 \cdot \lambda$ is the critical angle of bulk nickel in degrees with the wavelength λ in Å. Nowadays, *m*-values as high as $m = 8$ have been successfully achieved for Ni/Ti SMs [2], which in fact can extend the use of reflection optics from cold to thermal and epithermal neutrons, contributing to thermal neutron transport and focusing applications. Although such high *m*-values represent the current technological frontier for specialized optics, they remain exceptional; the standard *m*-value for the vast majority of neutron guide systems produced worldwide typically ranges between $m = 2$ and $m = 4$.

Supermirrors of Ni/Ti find application in neutron guides and focusing devices in order to achieve appreciable flux gains. Neutron guides are smooth-wall tubes whose inner surfaces are coated with neutron reflecting materials. When a neutron beam hits the surface of the guide at a shallow angle below a critical angle, $\theta_{\mathrm{crit,SM}}$, it undergoes total reflection and neutrons travel inside the guide without any remarkable loss.

As the required number of Ni/Ti double layers is proportional to $\approx 4.5\ \mathrm{m}^4$ [3,4], the supermirror structures develop stress and embrittlement with increasing *m*-value, resulting in low reflectivity due to large interface roughness and interdiffusion when sputtered in pure argon atmosphere [5]. Therefore, reactive sputtering of the Ni layers with a reactive gas (like synthetic air or N_2) was employed by different groups to produce large *m*-value supermirrors [2,5].

There is a list of well known effects which appear when adding reactive gases (like air or N_2) to the Ni sputtering process, like Ni lattice dilatation, reorientation of the Ni grains from the direction (111) to the (020), reduction of the grain size, smoothing of the layer surfaces,

* Corresponding author.
E-mail addresses: jose.gomez@frm2.tum.de (J.M. Gómez-Guzmán), s.puetter@fz-juelich.de (S. Pütter).

https://doi.org/10.1016/j.nima.2026.172078
Received 27 April 2026; Received in revised form 2 September 2026; Accepted 8 September 2026
Available online 14 September 2026
0168-9002/© 2026 The Authors. Published by Elsevier B.V. This is an open access article under the CC BY license (http://creativecommons.org/licenses/by/4.0/).
Open access funding enabled and organized by Projekt DEAL.

sharpening of the multilayer interfaces and suppression of Ni diffusion into Ti (e.g. [6]). All these effects yield a higher neutron reflectivity of Ni/Ti SMs [5,7]. However, though very important, these studies mainly focused on the neutron reflectivity, and lack a detailed investigation of the microstructural evolution and mechanism of Ni/Ti multilayers with reactive-gas incorporation.

In recent years, efforts have been devoted to explain the physical mechanism of the microstructural changes observed in Ni/Ti multilayers as a result of the incorporation of reactive gases like N_2 to the nickel layers. Feng et al. [8] have studied the microstructural evolution of Ni/Ti SMs with $m = 3$ based on the investigation of the interfacial roughness, crystallization, and stress of Ni/Ti multilayers with reactive-gas incorporation of nitrogen at different thicknesses.

In the present publication, we want to go one step further by applying the stress minimization to Ni/Ti SMs with increasing m-value achieved by the Neutron Optics Group of FRM II (Garching, Germany) [9]. Nickel thin layers and Ni/Ti SMs with m-values up to $m = 5$ were produced using an in-house DC magnetron sputtering system. As first step 800 Å Ni thin layers were sputtered at different deposition conditions by varying the flow rate of the reactive gas. Once the optimum flow rate was found, i.e. the minimum grain size and roughness of the Ni thin layers was reached, the Ni/Ti SMs were produced under the same conditions utilizing, when needed, the knowledge of optimized Ti layer growth [10].

A wide variety of experimental techniques was utilized, like X-ray Reflectivity (XRR) and Atomic Force Microscopy (AFM) to study the evolution of the surface roughness and X-ray Diffraction (XRD) to identify the formation of different crystal structures. Also, the XRD data were used to determine the residual stress in the Ni thin films by the $\sin^2\psi$ technique. The stress in the Ni thin films was corroborated with the wafer curvature method, which was also used to determine the stress in the Ni/Ti SMs. The resistivity of the Ni thin film samples was measured using a four-point-probe at room temperature. Neutron reflectometry measurements were used to check the reflectivity of the Ni/Ti SMs produced.

2. Experimental

2.1. Sample preparation

All samples were produced using an in-house magnetron sputtering system. The system is equipped with turbo molecular pumps backed with rotary pumps, with two magnetron cathodes, onto which two sputtering targets with dimensions 279 × 74 × 3 mm^3 are mounted. Each cathode is connected to a 2 kW DC power supply TruPlasma DC 3002 manufactured by TRUMPF Hüttinger GmbH (Germany). The distance between the surface of the substrate and the target was approximately 60 mm. In such a deposition system, the substrate is mounted onto a carrier which moves linearly underneath the sputtering targets, which are fixed. Therefore, the thickness of every layer is given by the deposition time, which is controlled by the speed of the carrier, and by the power provided at the magnetron cathodes. High purity Ni 99.99 % and Ti 99.6 % targets manufactured by Metallic Flex GmbH (Germany) were used for deposition.

Nickel thin films and Ni/Ti neutron SMs with different m-values were sputtered at constant power of 800 W (Ni) and 750 W (Ti) onto borosilicate float (Borofloat® 33) glass manufactured by Schott AG (Germany) [11], with dimensions 200 × 50 × 1 mm^3 (for residual stress measurements) and 200 × 50 × 11 mm^3 (for reflectivity measurements) in normal and polished quality. The layer sequence for the SMs with gradually varying layer thicknesses was calculated using the algorithm of Masalovich [12]. Synthetic air (80% N_2 + 20% O_2, purity 99.9995%) and argon (purity ≥ 99.995%) were used as reactive gas and working gas, respectively, to sputter the Ni thin films and the Ni/Ti SMs. To eliminate the dependence on the sputtering pressure, the total pressure was kept constant at 2×10^{-6} bar, equivalent to 40 sccm total gas flow rate. The flow rate of the synthetic air varied between 1 sccm and 23 sccm and the Ar flow was adjusted accordingly.

Initially, several 800 Å Ni thin films were sputtered at different deposition conditions by varying the flow rate of the reactive gas. Once the optimum flow rate was identified, sets of Ni/Ti SMs with different m-values comprising $m = 3$ to 5 were deposited under these conditions. For completeness, a set of Ni/Ti SMs with $m = 2.0$ to 2.8 was deposited by non-reactive DC sputtering. The thickness of the individual layers ranged from 28 Å (innermost layer) to 850 Å (outermost layer).

2.2. Sample characterization

XRR measurements were performed to investigate the density, thickness and surface roughness of the Ni thin layers. The scans were carried out in $\theta - 2\theta$ mode within a 2θ range of $0° - 3°$ with a laboratory X-ray reflectometer Bruker D8 operated at 40 kV, 40 mA, and equipped with a Cu-K_α X-ray source (1.54 Å wavelength). The crystalline structure of the thin films was investigated by XRD using the same instrument, but the scans were carried out in $\theta - 2\theta$ mode within a 2θ range of $30° - 60°$, with 0.025° step size and 40 s measuring time. The residual stress in the thin films was calculated by the $\sin^2\psi$ technique, as explained elsewhere [13,14]. Here, ψ is defined as the angle between the normal to the sample surface and the normal to the diffracting planes. This technique calculates the residual stress existing in the surface layer of polycrystalline materials by assuming a plane-stress state. Once the diffraction peaks have been fitted and the corresponding Bragg's angles determined, the d-spacing $d_\psi^{(hkl)}$ of a certain plane family (hkl) for a given ψ angle can be calculated using the Bragg's law. The residual strain $\varepsilon_\psi^{(hkl)}$ is then given by:

$$\varepsilon_\psi^{(hkl)} = \frac{d_\psi^{(hkl)} - d_0^{(hkl)}}{d_0^{(hkl)}}, \tag{1}$$

where $d_0^{(hkl)}$ is the d-spacing for a non-strained sample taken from the ICSD (Inorganic Crystal Structure Database). With the $\sin^2\psi$ method, the stress σ_ψ is given by [15]:

$$\sigma_\psi = \frac{E^{(hkl)}}{1+\upsilon} \cdot \frac{\delta\varepsilon_\psi^{(hkl)}}{\delta \sin^2\psi}, \tag{2}$$

where $E^{(hkl)}$ and υ are the Young modulus and the Poisson's ratio of the (hkl) planes, respectively, while the term $\frac{\delta\varepsilon_\psi^{(hkl)}}{\delta \sin^2\psi}$ represents the slope of the linear regression between $\varepsilon_\psi^{(hkl)}$ and $\sin^2\psi$. Therefore, the $\sin^2\psi$ method implies the measurement of strains for different tilting angles ψ. The d-spacing for non-stressed samples were taken from the reference patterns 260169-ICSD (fcc type structure Ni with space group Fm3m) and 9986-ICSD (fcc type structure NiO with space group Fm3m). Also, the Young modulus and the Poisson ratio are taken from literature. For Ni: $E^{(111)}$ = 294 GPa [16], $E^{(020)}$ = 125 GPa [17] and υ = 0.3 [18]. For NiO: $E^{(111)}$ = 166 GPa, $E^{(020)}$ = 146 GPa and υ = 0.385 [19].

The stress in the Ni thin films was also determined by the wafer curvature method, using an electronic autocollimator (TriAngle) to measure the curvature radii of the substrates before and after coating. For each 200 mm long sample, a laser beam was reflected from the sample surface at 10 positions along the longitudinal x-axis, spaced 20 mm apart, and the angular deviation θ of the reflected beam with respect to the center of the autocollimator was recorded at each position. A least-squares fit was then applied to the 10 measured points using the function $f(x) = k + \arcsin(x/R)$, where x is the position along the sample length, and R (curvature radius of the substrate) and k (offset of the measurement) are the fitting parameters. Once the curvature radii of the samples before and after the nickel coating are known, the value of the film stress can be calculated using the Stoney equation [20]:

$$\sigma_{\text{film}} = \frac{1}{6} \cdot \left(\frac{1}{R_{\text{post}}} - \frac{1}{R_{\text{pre}}}\right) \cdot \left(\frac{E}{1-\upsilon}\right) \cdot \frac{t_s^2}{t_c}, \tag{3}$$

where t_s is the thickness of the substrate, t_c is the total thickness of the film, R_{pre} and R_{pos} are the curvature radii of the substrate before and after coating, and E and υ are the Young modulus (E = 64 GPa) and Poisson's ratio (υ = 0.2) of Borofloat® 33, respectively [11].

The sheet resistance of the Ni thin films was measured using a four-point-probe Cascade Microtech (C4S-54/5) at room temperature. Therein, four equidistant tungsten carbide tips with a spacing of 1 mm and tip radii of 125 µm are placed on the thin film. Tips are mounted on a spring to prevent piercing of the thin film samples. A current (I) is applied on the outer two tips, while the inner two tips measure the induced voltage (U). The current was swept from −0.001 A to 0.001 A with step width of 10^{-5} A in 200 steps. The sheet resistance R_{sh} can then be calculated as $R_{sh} = ((\pi/ln(2)) \cdot U)/I$, and the resistivity as $\rho = R_{sh} \cdot t_c$, with t_c being the total thickness of the thin film sample.

Atomic Force Microscopy (AFM) measurements were performed with a Keysight 5500 instrument in tapping mode utilizing standard AFM probes (HQ:NSC15/Al BS by MikroMasch) in air. Prior to measuring, the surfaces were cleaned in ethanol and isopropanol. If necessary, the surfaces were further treated with a commercial silicone remover consisting of hydrocarbons C7–C9, n-alkanes, isooctane, cycloalkanes (R)-p-mentha-1,8-diene and 1-methoxy-2-propanol. Several images of 5 µm × 5 µm size were taken of each sample. The root mean square surface roughness σ_{AFM} was calculated with the data visualization and analysis software Gwyddion [21].

Neutron beam reflectivity measurements were performed using the reflectometers NARZISS at the spallation neutron source SINQ of Paul Scherrer Institute (PSI, Switzerland) [22] and REF at the Budapest Neutron Center (BNC, Hungary) [23].

All measurements throughout the publication were performed at room temperature and under ambient conditions.

3. Results and discussion on nickel thin films

3.1. Effect of the reactive gas on the surface roughness

A series of 800 Å Ni thin films were deposited on Borofloat® 33 glass substrates with varying air-flow. The samples were measured with XRR and the data were fitted by GenX [24], using density, thickness and roughness of the thin films as fitting parameters. In accordance with our own measurement statistics, the density and roughness of the glass substrates were allowed to vary in the range (2.27 ± 0.28) g/cm^3 and (7.8 ± 0.6) Å, also in agreement with the information from the supplier (2.23 g/cm^3 [11] and < 10 Å [25]). The obtained XRR density and surface roughness σ_{XRR}, along with the rms surface roughness σ_{AFM} determined by AFM are displayed in Fig. 1. For the Ni thin film, the density of pure nickel of 0.0914 at /Å^3 [26,27] was used as start point. The thin film density decreases with increasing air-flow (red squares) from 0.090 at /Å^3 for samples sputtered with an air-flow up to 3.5 sccm, to 0.079 at /Å^3 for the sample sputtered with highest air-flow. The trend reveals the formation of NiO as the air-flow increases, which will be explained in the following sections. The values found for the samples sputtered up to 3.5 sccm air-flow are compatible with the density of pure nickel of 0.0914 at /Å^3, while the value obtained for the sample sputtered with the highest air-flow approaches the density of pure NiO of 0.0554 at /Å^3 [28].

The XRR surface roughnes σ_{XRR} shows a clear dependence on the flow of synthetic air (black triangles, solid line), with a minimum of around 12 Å at an air-flow between 10 sccm to 12.5 sccm. Highest surface roughness is found in the Ni thin film sample sputtered in the absence of air. According to [6] non-reactively sputtered Ni thin films tend to develop rough interfaces due to large grains with preferred (111) orientation. Columnar growth of the Ni layer occurs and leads to rough interface. Senthil Kumar et al. [5] have studied the influence of adding synthetic air during sputtering of Ni single layers, Ni/Ti multilayers and Ni/Ti SMs. They observed a minimum surface roughness of 9 Å for Ni/Ti supermirrors above a certain air pressure threshold. Please note that due to different sputtering specifications the comparison of pressure and air-flow is only possible for the same sputtering system. Hence, no values are given here on purpose. However, all samples of Senthil Kumar et al. which were produced above this threshold, exhibited serious embrittlement, revealing the necessity of a further systematic study of the influence of synthetic air on Ni growth, which will be presented in the following.

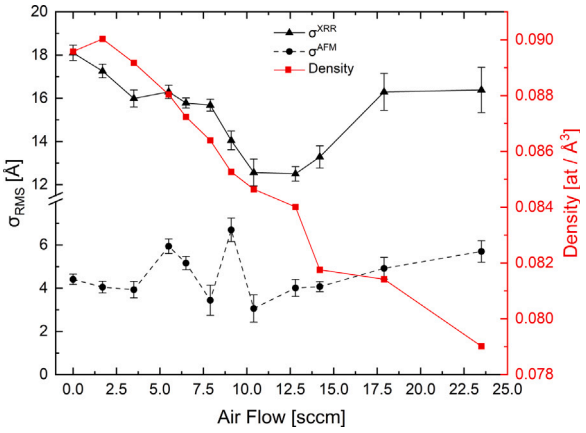


Fig. 1. Surface roughness of 800 Å Ni thin films deposited on Borofloat® 33 glass at different flow rates of synthetic air during deposition as calculated from XRR fitting (black triangles, solid line) and as measured via AFM (black dots, dashed line). The evolution of the density as calculated from XRR fitting is also shown (red squares).

Gaewdang et al. reported similar roughness improvement for copper oxide thin films with oxygen flow [29]. Increasing the oxygen flow from 2 sccm to 8 sccm in their sputtering instrument the AFM rms roughness decreased from 3.82 nm to 1.75 nm. The authors interpreted this roughness dependence as a non-optimal reactive gas concentration hindering the film from crystallization. During the sputtering process the reactive gas atoms are reflected from the target and hit the substrate with appreciable energy, thereby causing nucleation. Further increase of reactive gas flow may deplete metal atoms at the substrate, thereby inhibiting proper film nucleation and subsequent growth.

In contrast to the XRR surface roughness of the Ni films, the AFM rms roughness is lower and rather constant with an average value of σ_{AFM} = 4.62 ± 1.09 Å (black dots and dashed line in Fig. 1). Different values are also observed for the Borofloat® 33 glass substrates (σ_{AFM} = 3.32 ± 0.24 Å versus σ_{XRR} = 7.8 ± 0.6 Å). In any case the film roughness is close to the substrate roughness, revealing high quality films.

The different magnitude of the AFM roughness with respect to the XRR roughness can be explained by the fact that AFM bases on the interaction force between the microscope's tip and the sample surface while XRR probes its electron density profile. Also probing different sizes of surface areas, i.e. a few mm^2 for XRR versus µm^2 for AFM or varying size of the scanning area itself for AFM have an impact [30,31]. For XRR, the model for the surface roughness plays a significant role for the validity of the fit [32,33]. The minimum of σ_{XRR} in the range of 10 sccm to 12.5 sccm airflow is considered as an indication for optimum film preparation and will be discussed further in the following section.

3.2. Structural properties

Fig. 2 displays XRD patterns of the Ni thin films deposited at different flow rates of synthetic air. The Rietveld refinement of the XRD data was performed with the software HighScore Plus 5.1 using pseudo-Voigt functions [34]. For the film deposited under pure argon atmosphere, two diffraction peaks appear, a strong one (111) and a tiny one (020) at the 2θ angles of 44.50° and 51.85°, respectively.

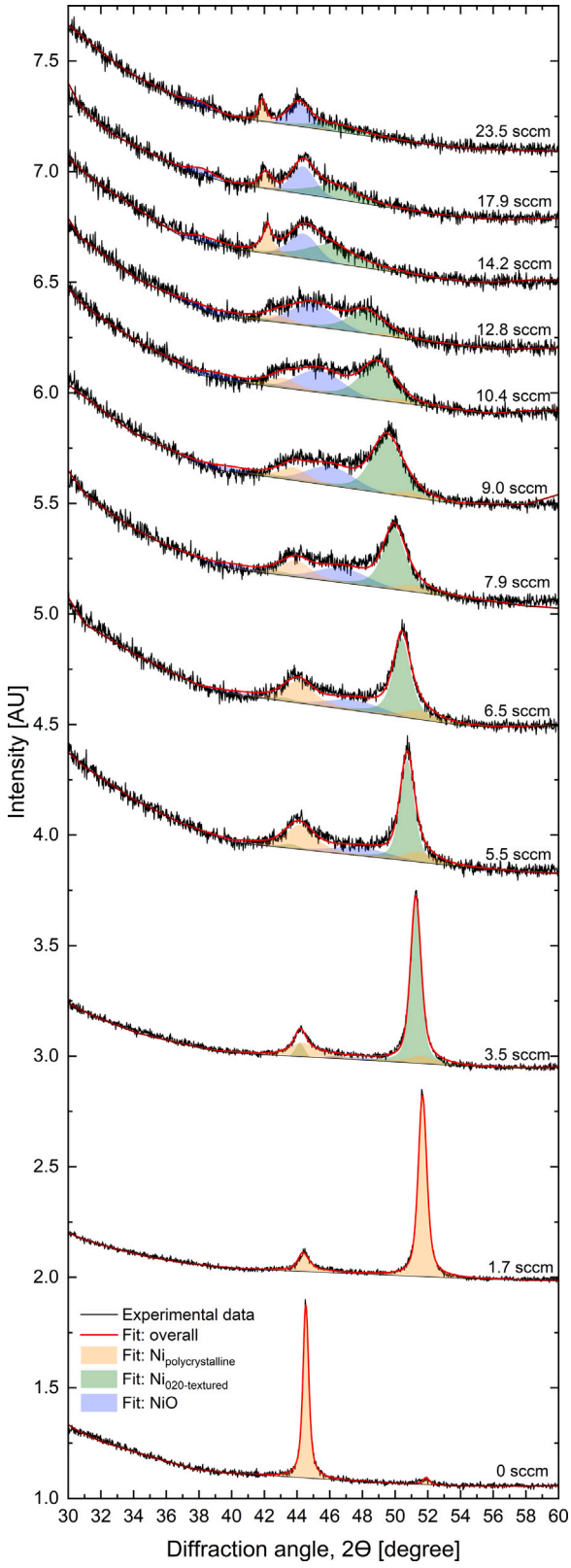


Fig. 2. XRD patterns of 800 Å nickel thin films with increasing flow rates of synthetic air during deposition. Black line: experimental data. Red line: overall fit. Orange area: reference pattern 260169-ICSD (polycrystalline fcc Ni) fit. Green area: reference pattern 260169-ICSD ((020)-textured fcc Ni) fit. Blue area: reference pattern 9866-ICSD (fcc NiO) fit.

The peaks, depicted as orange areas in Fig. 2, are identified to refer to polycrystalline fcc Ni with space group Fm3m (Ref. Pattern: 260169-ICSD). The sharp peaks indicate high crystallinity, with interplanar d-spacing constants of 2.035 Å and 1.762 Å for the (111) the (020) peaks, respectively, close to the bulk values (2.037 Å and 1.764 Å, given by crosses in Fig. 3a and 3b). The variation of the interplanar d-spacing with the flow rate is given in Fig. 3. On increasing the flow rate of synthetic air up to 3.5 sccm, there is a coexistence of polycrystalline fcc Ni with strongly (020)-textured fcc Ni (green areas in Fig. 2), for which the weight relation changes with the air-flow as depicted in Fig. 4. On increasing air-flow, fcc NiO (blue areas in Fig. 2) with space group Fm3m (Ref. Pattern: 9866-ICSD) coexists with the fcc Ni, changing its weight fraction with the air-flow (see Fig. 4). At highest air-flow the peaks of Ni have nearly vanished and mostly the fcc NiO remains. In general, the peaks in Fig. 2 shift towards lower angles, reflecting an increase of the d-spacing constant as shown in Fig. 3. The d-spacing for the (111) and the (020) peaks of polycrystalline Ni increases from 2.035 Å to 2.159 Å and from 1.764 Å to 1.871 Å (Fig. 3a). The d-spacing for the (111) and the (020) peaks of 020-textured Ni increases from 2.007 Å to 2.253 Å and from 1.750 Å to 1.951 Å (Fig. 3b), while the d-spacing for NiO rises from 2.197 Å to 2.373 Å and from 1.903 Å to 2.051. The final values for NiO are close to the bulk values (2.412 Å and 2.089 Å, given by crosses in Fig. 3c).

Fig. 4 shows the weight percentages of Ni and NiO in the Ni thin films as a function of the flow of synthetic air, obtained from the fitting of the XRD data. Without air-flow only polycrystalline Ni with preferred (111) orientation (orange solid bar) exists. On increasing the air-flow, the samples remain polycrystalline fcc Ni, but with a preferred (020) orientation (orange dashed bar). At 3.5 sccm of air-flow, the samples become a mixture of polycrystalline fcc Ni and a strongly (020)-textured fcc Ni (green dashed bar), while the fcc NiO with preferred (020) orientation starts to appear (blue dashed bar). Above that air-flow, these three components remain present but their weight percentage varies. The NiO content increases, specially the (020) orientation, while simultaneously, the fcc Ni weight percentage decreases. Both orientations (111) and (020) of polycrystalline fcc Ni almost vanish above 14 sccm air-flow. Evidently, the oxidation of the Ni layer proceeds continuously. For the minimum surface roughness as determined by XRR, i.e. between 10 sccm and 12.5 sccm air-flow, the weight percentage of Ni and NiO is about 50% each. At maximum air-flow, polycrystalline fcc Ni and (020)-textured Ni have almost vanished and mainly NiO (020) is present in the sample.

In Fig. 5 the average grain size L for the different crystalline structures is shown. The values were derived from the broadening of the diffraction peaks depicted in Fig. 2 using the Scherrer equation ($L = K\lambda/\beta\cos(\theta)$), with λ being the wavelength of the X-rays, θ the angular position, β the full width at half maximum (FWHM) of the diffraction peak and K the shape factor of the scattering grains, set to 0.94 [35]. The grain size obtained from the Scherrer analysis corresponds to the direction oriented parallel to the sample normal. In general, large FWHM of the diffraction peak corresponds to small grain size. For polycrystalline fcc Ni the grain size first decreases with increasing air-flow (Fig. 5a). At about 5 sccm the grain size exhibits a plateau and then increases again for air-flows higher than 13 sccm. This behavior is observed independent of the crystalline orientation, with grain sizes ranging from 25 nm without reactive gas to minimum 5 nm at 5–12 sccm air-flow rate. For (020)-textured fcc Ni the grain size of both (111) and (020) orientations gradually decreases from 14 nm to 2.7 nm at the air-flow of 13 sccm (Fig. 5b). For NiO, grains evolve at about 3.5 sccm (Fig. 5c). For both (111) and (020) orientations the grain size gradually increases from 2.2 nm to 2.8 nm at the air-flow of 13 sccm. Afterwards, a stronger increase in grain size to 6 nm for maximum air-flow is found. This observation is in agreement with findings of Elsenhans et al. [6]. It is worth mentioning that the air-flow window of minimized surface roughness coincides with the minimum grain sizes of polycrystalline Ni and NiO, while the grains of (020)-textured fcc Ni are of 3.9 nm, as compared to their minimum size of 2.7 nm. Obviously, the optimum composition is gained if all grains are of approximately the same size.

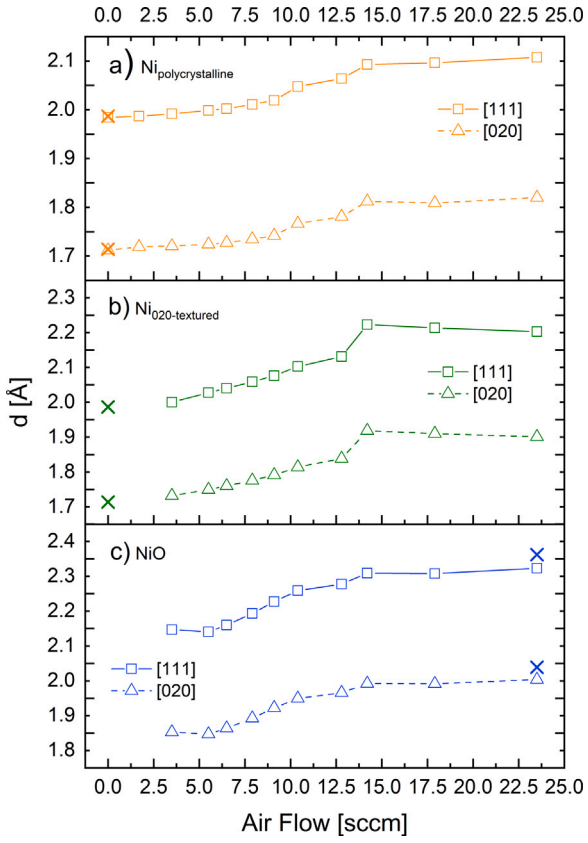


Fig. 3. Variation of the interplanar d-spacing of the different Ni crystal structures with increasing flow rates of synthetic air during deposition. Diffraction peaks (111) (squares, solid line) and (020) (triangles, dashed line) are shown for polycrystalline fcc Ni (a), (020)-textured fcc Ni (b) and fcc NiO (c). The crosses in (a) and (b) are the bulk interplanar d-spacing of fcc Ni (Ref. Pattern: 260169-ICSD). The crosses in (c) are the bulk interplanar d-spacing of fcc NiO (Ref. Pattern 9866-ICSD).

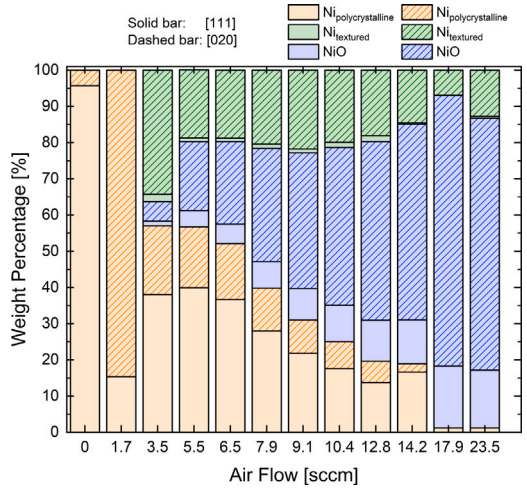


Fig. 4. Weight percentage evolution of the different crystalline structures with increasing flow rates of synthetic air during deposition as given by HighScore Plus 5.1. Orange: polycrystalline Ni. Green: 020-textured Ni. Blue: NiO. Solid bar: (111) orientation. Dashed bar: (020) orientation.

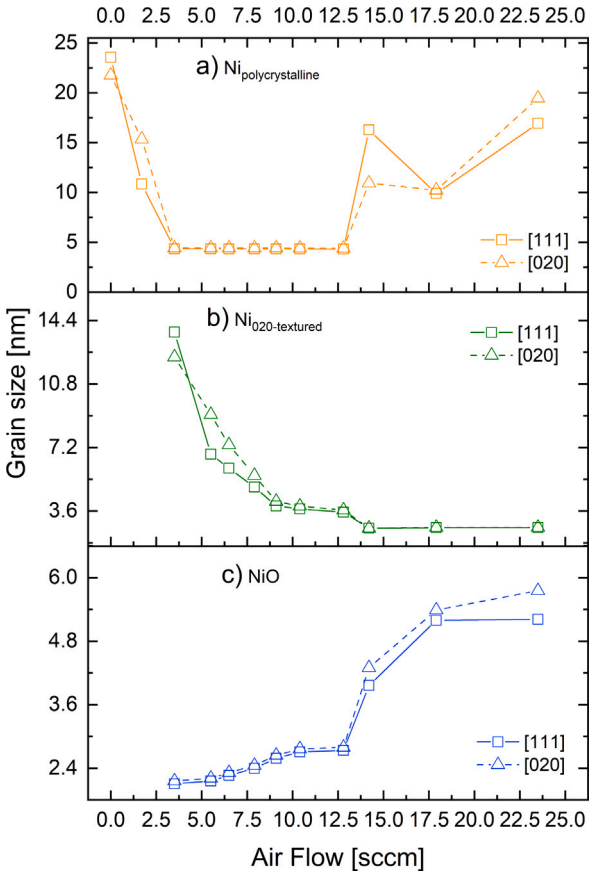


Fig. 5. Grain size evolution of the different Ni crystal structures with increasing flow rates of synthetic air during deposition. Diffraction peaks (111) (squares, solid line) and (020) (triangles, dashed line) for polycrystalline fcc Ni (a), (020)-textured fcc Ni (b) and fcc NiO (c).

3.3. Electrical properties

The resistivity of the Ni films is plotted as a function of the flow rate of synthetic air in Fig. 6. At zero air-flow the lowest resistivity of 11.6 μΩ·cm is measured. This value is similar to the values of Bakonyi et al. [36] and references therein but 60% higher than the resistivity of the defect-free bulk nickel (7.24 μΩ·cm), as given by [37]. Bakonyi et al. explain the higher value by the existence of an additional grain-boundary contribution due to Ni crystallites. With synthetic air the resistivity continuously increases up to 190 μΩ·cm at 23 sccm and agrees well with literature [5]. The behavior can be explained by a gradually increasing interstitial occupancy of oxygen in the Ni lattice and the creation of the new phase NiO, which is an insulator. This finding is supported by the XRD measurements, as NiO is observed to form at a flow rate of 3.5 sccm. Hence, the resistance in the Ni thin films increases due to the increase of electron–impurity scattering. Additionally, the interstitial oxygen occupancy leads to a local distortion of the Ni lattice as shown by the increase in planar d-spacing of Ni with increasing flow rate of synthetic air (Fig. 3). All contributions from the impurity, the creation of the new phase NiO and the distorted lattice increase the resistance of the Ni thin films.

3.4. Residual stress

The growth of Ni thin films on the glass substrates may result in large thin film stress and furthermore to its delamination from the substrate surface, thus degrading its physical structure. Therefore, one

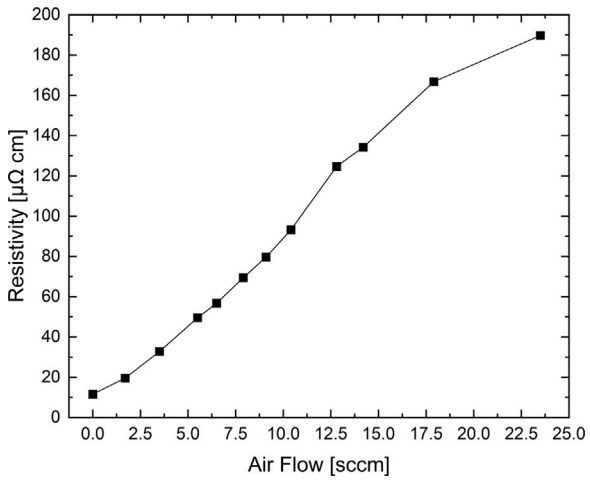


Fig. 6. Resistivity evolution in Ni thin film samples as a function of the flow rate of synthetic air during deposition.

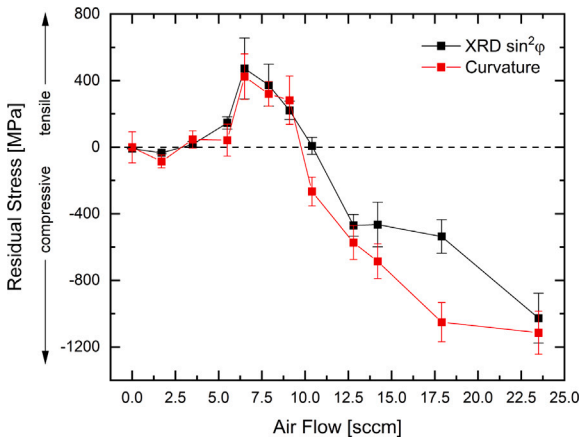


Fig. 7. Variation of the mechanical stress in Ni thin film samples as a function of the flow rate of synthetic air during deposition as calculated from the XRD $\sin^2\psi$ method (black curve) and from the curvature method (red curve). The black curve represents the sum of the weighted (vol.%) stresses in the individual nickel crystalline directions (111) and (020) for the structures polycrystalline Ni, 020-textured Ni and NiO.

of the performance indicators used to optimize the quality of the Ni thin films is the control of the stress.

The residual stress in the Ni thin films was measured via XRD and wafer curvature technique as function of the flow rate of synthetic air, see Fig. 7. The XRD measurements are evaluated by the $\sin^2\psi$ method [13,14]. Details are given in Section 2.2. The XRD measurements were performed for different angles in the ψ range -10° to 10°, similar to the range −13.5° to 10° of [38]. As only the volume average of the residual stress is determined [39], the stress shown in Fig. 7 (black squares) represents the sum of the weighted (vol.%) stresses in the individual nickel crystalline directions (111) and (020) for the structures polycrystalline Ni, 020-textured Ni and NiO.

For comparison, the stress was also investigated using the wafer curvature method (red squares). The measurement of the curvature radii of the Borofloat substrates before and after the coating were conducted using an electronic autocollimator, as described in Section 2.2. Both methods reveal very similar behavior over the full air-flow range. Increasing the air-flow, the tensile stress increases with a maximum of 450 MPa at about 7.5 sccm and then decreases to compensation of stress at around 10 sccm. Further air-flow increase leads to compressive stress with rather constant value of about −1000 MPa for the wafer curvature method. The $\sin^2\psi$ method provides systematically lower values than the wafer curvature method in the compressive side. This discrepancy has already been reported by [40] based in the fact that it is a local, surface-sensitive measurement, whereas the wafer curvature method measures a global, volume-averaged stress for the entire film–substrate system. Other authors explain this difference in how the X-ray penetration depth and anisotropic elastic constants create variations that the curvature method averages out [41] and in why diffraction averages differ from mechanical averages due to grain interaction and texture [42].

The stress evolution can be attributed to the incorporation of synthetic air during the sputtering of the Ni layers. At low air-flow rates below 3.5 sccm, interstitial site occupancy remains negligible, and hence, the stress is not significantly altered, i.e. those samples are stress-free. At about 3.5 sccm NiO is formed, which is known to drive tensile stress [43]. As the flow rate of synthetic air further increases to 7.5 sccm, the tensile stress increases to maximum 450 MPa. On further increase of the air-flow a sharp transition to compressive stress occurs at around 10 sccm, surpassing a maximum value of −1000 MPa. This reversal is driven by the nitrogen and oxygen atoms producing large local lattice expansions (as shown in Fig. 3), which leads to high compression in the host Ni lattice. Moreover, these large local strains can also lead to structural transformation and/or amorphization of the Ni layers [44].

Sentil Kumar et al. [5,45] reported similar stress behavior in 1000 Å Ni film samples which were reactively sputtered at different air pressures, with tensile stress ranging from 250 MPa at low air pressure to compressive stress of −1000 MPa at high air pressure. Zhang at al. [20] also observed a similar transition from compressive to tensile stress in Ni/Ti periodic multilayer samples prepared by DC sputtering when nickel layers were reactively produced in different nitrogen atmospheres.

Both XRD $\sin^2\psi$ and wafer curvature measurements indicate that the residual stress in Ni film also approaches a neutral state at near-zero air-flows. This suggests that the stress minimization may be achieved either by using low air-flows or by selecting the transition point from tensile to compressive. As a proof of principle, a 480-layer supermirror with *m*-value 3.0 was deposited under near-zero air-flow. It exhibited peeling-off even before the deposition process was complete, which is attributed to an insufficiently minimized grain size. Considering in conjunction the air-flow dependence of the surface roughness (Fig. 1), the grain size (Fig. 5) and the residual stress (Fig. 7), it is evident that the minimization of the grain size effectively reduces the internal stress of the nickel thin film samples; this minimum grain-size condition coincides with the minimum in surface roughness. All the results obtained suggest that the air-flow interval, where the transition from tensile to compressive stress takes place, is most suitable for producing Ni/Ti SMs, as high reflectivity and mechanical stability of the layers are expected. Hence, the air-flow of 10 sccm is considered as optimum value.

4. Results and discussion on Ni/Ti supermirrors

Based on the results for Ni thin films and our optimization results for Ti thin films published in [10], Ni/Ti SMs with *m*-values between 3 and 5 were prepared by reactive DC sputtering under the optimum, stress-free condition, i. e. with 10 sccm flow of synthetic air on Borofloat® 33 glass substrates of 1 mm (for residual stress measurements) and 11 mm (for reflectivity measurements) thickness. For completeness, Ni/Ti SMs with *m*-values below 2.8 were produced by non-reactive DC sputtering. Further sample specifications can be found in Table 1.

Table 1
Overview of the Ni/Ti SMs with varying *m*-value and their fabrication properties, *n* is the number of layers, t_c is the total thickness. Ni denotes nickel and Ti denotes titanium. The substrate is always Borofloat® 33 glass, either of normal surface roughness or polished.

m	n	t_c [μm]	Ni	Ti	Substrate
2.0	106	1.2	Non-reactive	Non-reactive	Normal
2.5	240	2.0	Non-reactive	Non-reactive	Normal
2.8	370	2.7	Non-reactive	Non-reactive	Normal
3.0	480	3.3	Reactive	Non-reactive	Normal
3.5	804	4.6	Reactive	Non-reactive	Normal
4.0	1164	5.2	Reactive	Non-reactive	Normal
			Reactive	Non-reactive	Normal
5.0	1314	5.9	Reactive	Reactive	Normal
			Reactive	Reactive	Polished

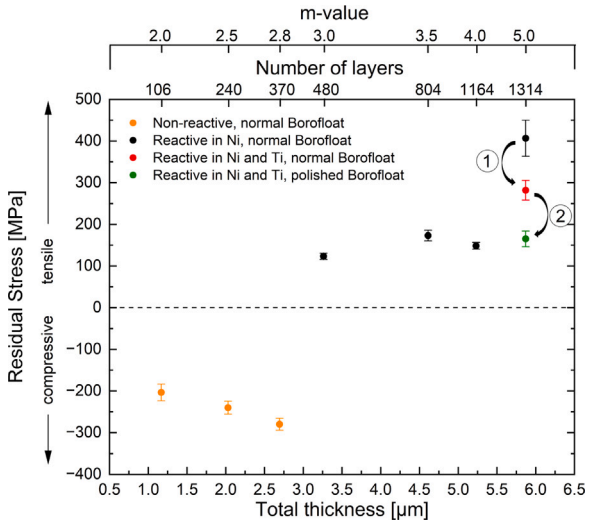


Fig. 8. Variation of the residual stress in Ni/Ti SMs with different total thicknesses. Samples represented by orange dots are non-reactively DC-sputtered on normal Borofloat® 33 glass substrates. The black dots represent SMs with reactively DC-sputtered Ni at 10 sccm air on normal Borofloat® 33 glass substrates. The sample represented by the red dot was reactively DC-sputtered also in the Ti layers at 3 sccm air on the same glass substrate (path 1). The sample represented by the green dot was reactively DC-sputtered in the Ni and Ti layers on polished Borofloat® 33 glass substrate (path 2).

4.1. Residual stress

Peeling-off (i.e. delamination) of multilayers/SMs from the glass substrate occurs when the total force acting on the substrate exceeds the shear strength of the film–substrate interface; i.e. an adhesive failure. To improve the coating's durability it is desirable that it is in a zero stress state or even in a slightly compressive stress state, as this counteracts the tensile forces that cause the delamination. However, high compressive residual stress also correlates to increased fracture toughness of the coated surface [46].

The wafer curvature method was applied to determine the stress in the neutron Ni/Ti SMs. The residual stress as a function of the total thickness and the *m*-value of the Ni/Ti SMs is shown in Fig. 8. Evidently, the stress in the SMs is dependent on non-reactive/reactive sputtering. Ni/Ti SMs deposited on normal Borofloat® 33 glass with non-reactive DC sputtering of Ni, i. e. those with $m < 3$, exhibit compressive stress which ranges from −200 MPa to −280 MPa (orange dots in Fig. 8). Also, the stress seems to follow a linear trend: the thicker is the multilayer, the higher is the compressive stress.

Considering the samples produced with reactive DC sputtering of the Ni layers on normal Borofloat® 33 glass substrates (black dots in Fig. 8), the residual mechanical stress becomes tensile, which is compatible with the formation of NiO driving tensile stress [43]. For the Ni/Ti SMs with *m*-values between 3.0 and 4.0, the stress ranges from 120 MPa to 180 MPa. Though the number of layers changes drastically from 480 layers to 1164 layers, the tensile stress does not differ considerably (mean value 148 ± 25 MPa). Further increase of the number of layers from 1164 ($m = 4$) to 1314 ($m = 5$) increases the residual mechanical stress by a factor of more than two, i. e. to a value of 410 MPa for $m = 5$.

At first sight it may appear counter-intuitive that stacking Ni layers grown under the optimum, stress-free condition, i. e. with 10 sccm flow of synthetic air, for which the single 800 Å Ni film shows a near-zero stress (Fig. 7), results in a measurable net tensile stress once assembled into a Ni/Ti SM. However, Senthil Kumar et al. [45] have shown the same behavior for a $m = 3$ Ni/Ti SM reactively sputtered. There it is shown that 1000 Å nickel layers are stress-free when reactively sputtered at $p_{air} = 0.1 \times 10^{-3}$ mbar and $p_{argon} = 0.73 \times 10^{-3}$ mbar, while titanium layers non-reactively sputtered at $p_{argon} = 0.44 \times 10^{-3}$ mbar shows compressive stress of around -700 MPa. When the same sputtering conditions are used to sputter a $m = 3$ Ni/Ti supermirror having around 500 layers, this shows a tensile total stress of around 200 MPa. If the stress in a multilayer is then the sum of the stresses in the individual Ni and Ti layers alone, then one would expect to observe compressive stress because the sum of the Ni and the Ti total stress is negative. In contrast, the resulting stress in the Ni/Ti SM is tensile. It is then presumable that the tensile stress in the Ni/Ti SM may arise, in addition to the formation of NiO driving tensile stress [43], from the interfaces, as stated by Senthil Kumar et al. [45]. According to Elsenhans et al. [6], sputtering reactively Ni layers leads to a suppression of the diffusion of Ni into Ti, which creates an interdiffusion-asymmetry as Ni-on-Ti and Ti-on-Ni interfaces are then not structurally equivalent. It is then possible that their individual stress contributions do not cancel even though both interface types occur with equal frequency. We believe that these are two plausible contributors to the residual stress observed in the SMs, though they are not yet disentangled; a layer-resolved investigation of this effect would still be needed.

All SMs with $m \leq 4$, which were DC-sputtered with reactive air at 10 sccm in the Ni layers on normal Borofloat® 33 glass substrates presented long term mechanical stability. However, for the SM of $m = 5$, the SM coating started to peel off a few days after the sample was produced, revealing that the residual mechanical stress exceeded the shear strength of the interface between the coating and the substrate. To further reduce the mechanical stress, reactive DC sputtering was also applied in the Ti layers with 3 sccm air-flow, which is known to reduce its roughness [10]. Consequently, the mechanical stress of the SM was reduced to 280 MPa (red dot in Fig. 8, path 1). This sample was mechanically stable over several weeks but then also peeled off, revealing that this level of stress still exceeded the shear strength of the interface between the coating and the substrate. As next step to produce a mechanically stable $m = 5$ Ni/Ti SM, polished Borofloat® 33 glass substrates with nominal roughness < 5 Å, as given by the manufacturer [25] and reactive sputtering of the Ni and Ti layers was used. The mechanical stress was successfully reduced to 165 MPa (green dot in Fig. 8, path 2), which is now comparable to the one in the $m = 3.5$ and 4 Ni/Ti SMs. Accordingly, a mechanically stable $m = 5$ Ni/Ti SM was successfully fabricated.

According to the literature, the act of polishing certain borosilicate glass compositions in an aqueous environment can reduce its elastic modulus *E* by around 20% [47], which might reduce the calculation of the stress according to Eq. (3), while it also reduces its adhesion properties [48]. Given that this reduction may not completely explain the reduction of almost a factor of two on the stress between the $m = 5$ SMs sputtered in normal and polished Borofloat® 33 glass substrates (280 MPa as compared to 165 MPa), there might exist other contributions. Part of this stress reduction may be related to the lower surface roughness of the polished glass, given that the grain size and roughness of the deposited layers are already minimized under

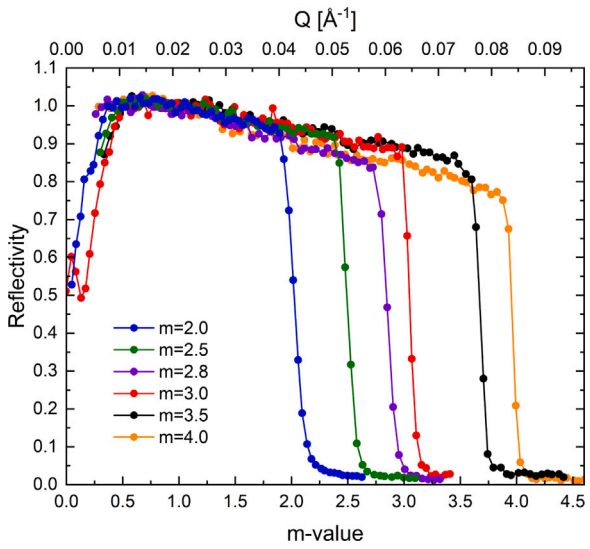


Fig. 9. Neutron reflectivity curves of Ni/Ti SMs deposited with non-reactive DC sputtering (m = 2, 2.5 and 2.8) and with reactive DC sputtering on Ni layers at 10 sccm air-flow (m = 3, 3.5 and 4.0). All samples were sputtered on normal 11 mm thick Borofloat® 33 glass substrates.

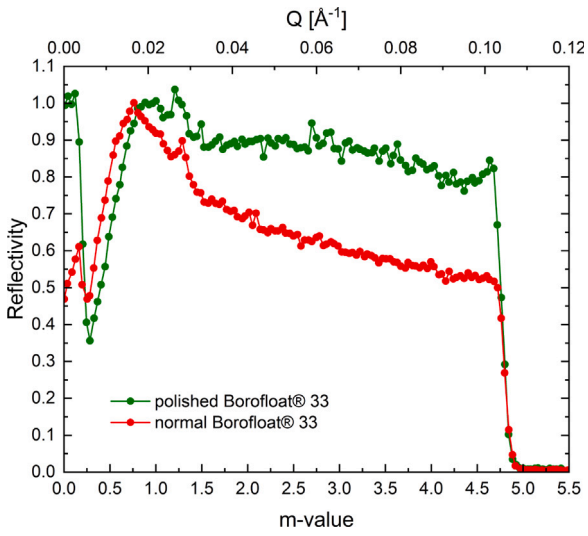


Fig. 10. Neutron reflectivity of m = 5 Ni/Ti SMs deposited with reactive sputtering in both the Ni and the Ti layers in normal Borofloat® 33 glass (red dots, path 1 in Fig. 8) and in polished Borofloat® 33 glass (green dots, path 2 in Fig. 8).

the optimized reactive DC-sputtering conditions applied to both substrates. However, differences in substrate mechanical properties and/or adhesion resulting from the polishing process, which were not independently characterized in this work, cannot be excluded as additional or alternative contributions to the observed stress reduction.

4.2. Neutron reflectivity

The reflectivity of all produced Ni/Ti SMs discussed in the section before was measured at the reflectometers NARZIS at SINQ (PSI, Switzerland) [22] and REF at BNC (Hungary) [23], with wavelengths λ = 5 Å and λ = 4.29 Å, respectively. Fig. 9 shows the reflectivity measurements of SMs with $2 \leq m \leq 4$ as a function of the Q vector, defined as $4\pi \sin(\theta)/\lambda$, and m-value. The slope of the reflectivity is similar for all m-values, e.g. SMs with $m = 2$ and $m = 4$ have essentially the same reflectivity at m = 2, which demonstrates that the growth mode of the layers does not change, i. e. the interface roughness remains essentially constant. Consequently, the performance of high m-value SMs is not compromised at low m-values. Therefore, the increase of the m-values leads to a real gain of intensity due to the increased divergence of the neutron beam.

In Fig. 10 the reflectivity of the m = 5 Ni/Ti SMs fabricated on different qualities of Borofloat® 33 glass substrates with Ni and Ti layers deposited with DC reactive sputtering is given (red dots: normal glass, path 1 in Fig. 8; green dots: polished glass, path 2 in Fig. 8). The gain of reflectivity due to the lower surface roughness of < 5 Å of the polished glass compared to the value of < 10 Å of the normal glass is evident. To understand this effect, we consider the surface roughness of the jth layer σ_j within a Ni/Ti SM of total thickness h with substrate roughness σ_s as given by [49],

$$\sigma_j(h)[\text{Å}] = \sigma_s[\text{Å}] + 0.1 \cdot h[\mu\text{m}]. \quad (4)$$

Here it is assumed that σ_j grows by 0.1 Å per μm of the deposited thickness h of the multilayer as measured from the substrate. As the thickness of the m = 5 SM is h =5.9 μm, it follows that the surface quality of the substrate is essential for the total roughness of the Ni/Ti SM. Moreover, a higher interface roughness reduces the reflectivity of a neutron SM through a mechanism analogous to the Debye–Waller factor that attenuates diffracted intensity in a crystal: both arise from a roughness/displacement-induced exponential attenuation term (Eq. (5)). The real (i.e. non-ideal) reflectivity R_{real} for the multilayer, accounting for the cumulative roughness σ_j of its interfaces, is then given as [50]

$$R_{\text{real}} = R_{\text{ideal}} \cdot e^{-(q_z^2 \cdot \sigma_j^2)}, \quad (5)$$

where R_{ideal} is the reflectivity with ideal, i. e. zero roughness and q_z is the q-vector. Accordingly, the surface roughness of the substrate is essential for high reflectivity supermirrors.

The reflectivity of the m = 5 Ni/Ti SM sputtered on normal Borofloat® 33 (red dots in Fig. 10) is fully governed by the excessive roughness of the multilayer. In contrast, while the m = 5 Ni/Ti SM sputtered on polished Borofloat® 33 (green dots in Fig. 10) exhibits a 30% higher overall reflectivity, it shows a 10% drop at approximately 0.03 Å^{-1}. This dip is attributed to a deficiency in the total number of layers in the multilayer structure. Taking into account that the number of layers for Ni/Ti SMs increases proportional to ≈ 4.5 m^4 [3,4], an m = 5 SM is supposed to possess more than 2000 layers, while the SM with m = 5 presented here only consists of 1314 layers, which is the maximum achievable number of layers with mechanical stability for the sputtering system at hand.

Attempts to fabricate a neutron SM with m = 5 and a higher number of layers (1560 layers and 6.3 μm total thickness) failed as the coating peeled off only a few hours after production, even when combining the reactive DC sputtering of both Ni and Ti layers with the use of polished Borofloat® 33 glass.

There are a few other techniques to improve the performance of high m-value Ni/Ti SMs in terms of stress minimization and higher neutron reflectivity, like applying a bias voltage to the substrate during the deposition [51], applying ion polishing to every Ni and Ti layer right after depositing [52] and introducing additional ultrathin layers of Cr at the Ni/Ti interfaces [53]. Unfortunately, none of these techniques can be implemented in the sputtering system used in this publication.

5. Conclusions

In this study the effect of synthetic air on the mechanical stress and the reflectivity of nickel thin films and Ni/Ti neutron SMs prepared via reactive DC magnetron sputtering was investigated.

XRR results on Ni thin films of 800 Å indicate an improvement of the surface roughness from 18 Å (no air-flow) to 12 Å (in the optimum air-flow of 10 sccm to 12 sccm). XRD measurements reveal in the film

deposited in pure argon atmosphere (no air-flow) the crystallization of polycrystalline fcc Ni with preferred (111) orientation. On increasing the air-flow, the samples are still polycrystalline fcc Ni, but this time with a preferred (020) orientation. At 3.5 sccm of air-flow, the samples are a mixture of polycrystalline fcc Ni and a strongly (020)-textured fcc Ni, while fcc NiO with preferred (020) orientation starts to appear. Above that air-flow, these three components remain present but their weight percentage varies. The NiO content increases, specially the (020) orientation, while simultaneously, the weight percentages of both the polycrystalline fcc Ni and the (020)-textured fcc Ni decrease. Above 14 sccm air-flow, polycrystalline fcc Ni has almost vanished and only (020)-textured fcc Ni and fcc NiO remains present.

The evolution of the nickel grain size as a function of the flow rate of synthetic air gives minimum grain size of about 5 nm and 2.7 nm for polycrystalline fcc Ni and 020-textured Ni, respectively, and low grain sizes from 2.2 nm up to 2.8 nm for NiO at air-flows below 13 sccm. The stress developed in the thin Ni films during the DC sputtering process approaches a neutral state at near-zero air-flows. As the flow rate of synthetic air increases to 7.5 sccm, the stress becomes tensile to maximum 450 MPa. On further increase of the air-flow a sharp transition to compressive stress surpassing a maximum value of −1000 MPa occurs, with stress compensation at around 10 sccm.

It was found that the effective reduction of the grain size effectively reduced the internal stress in the thin film samples; this reduction coincided with a reduction of the surface roughness. Thanks to this stress minimization, mechanically stable Ni/Ti SMs with m-values up to $m = 4$ were produced. To optimize a Ni/Ti SM with $m = 5$, a polished substrate and reactively sputtered titanium layers were utilized. The resulting specimen exhibited a stress level comparable to the $m = 4.0$ SM while remaining mechanically stable, though its overall reflectivity showed a 10% drop at approximately $0.03\,\text{Å}^{-1}$ attributed to a deficiency in the total number of layers in the multilayer structure.

CRediT authorship contribution statement

Jose Manuel Gómez-Guzmán: Writing – original draft, Visualization, Validation, Supervision, Resources, Project administration, Methodology, Investigation, Formal analysis, Data curation, Conceptualization. **Sabine Pütter:** Writing – original draft, Methodology, Investigation, Formal analysis, Data curation.

Declaration of competing interest

The authors declare that they have no known competing financial interests or personal relationships that could have appeared to influence the work reported in this paper.

Acknowledgments

The authors would like to thank the technicians of the Neutron Optics group of FRM II, Daniel Strobel and Senay Öztürk, for preparing the samples as well as Uwe Filges and Christine Klauser from the instrument NARZISS in PSI and Tamas Veres from the instrument REF in BNC for performing the reflectivity measurements on the Ni/Ti SMs. The authors also thank Simon Wegener, who performed the resistivity measurements with the 4-point-probe. Thanks are also given to Stephan Geprägs (Walther-Meißner-Institute for Low Temperature Research) for fruitful discussions on XRR and AFM. SP likes to thank Gerald Kada for supplying tips and tricks in AFM measurements.

Data availability

Data will be made available on request.

References

[1] J.B. Hayter, H.A. Mook, Discrete thin-film multilayer design for X-ray and neutron supermirrors, J. Appl. Crystallography 22 (1) (1989) 35–41, http://dx.doi.org/10.1107/S0021889888010003.

[2] C. Schanzer, M. Schneider, P. Böni, Neutron optics: Towards applications for hot neutrons, J. Phys.: Conf. Ser. 746 (1) (2016) 012024, http://dx.doi.org/10.1088/1742-6596/746/1/012024.

[3] T. Krist, A. Teichert, R. Kovács-Mezei, L. Rosta, Neutron supermirror development, in: A. Erko, M. Idir, T. Krist, A.G. Michette (Eds.), Modern Developments in X-Ray and Neutron Optics, Springer Berlin Heidelberg, Berlin, Heidelberg, 2008, pp. 355–370, http://dx.doi.org/10.1007/978-3-540-74561-7_22.

[4] P. Böni, Novel concepts in neutron instrumentation, Phys. B 276–278 (2000) 6–11, http://dx.doi.org/10.1016/S0921-4526(99)01355-1, URL https://www.sciencedirect.com/science/article/pii/S0921452699013551.

[5] M. Senthil Kumar, P. Böni, M. Horisberger, Relationship between neutron reflectivity, electrical resistance, stress and embrittlement in reactively sputtered Ni/Ti multilayers and supermirrors, Phys. B 385–386 (2006) 1265–1267, http://dx.doi.org/10.1016/j.physb.2006.06.027, URL https://www.sciencedirect.com/science/article/pii/S092145260601355X.

[6] O. Elsenhans, P. Böni, H. Friedli, H. Grimmer, P. Buffat, K. Leifer, J. Söchtig, I. Anderson, Development of Ni/Ti multilayer supermirrors for neutron optics, Thin Solid Films 246 (1) (1994) 110–119, http://dx.doi.org/10.1016/0040-6090(94)90739-0, URL https://www.sciencedirect.com/science/article/pii/0040609094907390, Special Issue: Frontiers in Thin Film Research.

[7] N. Abharana, A. Biswas, P. Sarkar, S. Rai, S. Singh, S. Kumar, S. Jha, D. Bhattacharyya, Effect of argon-nitrogen mixed ambient Ni sputtering on the interface diffusion of Ni/Ti periodic multilayers and supermirrors, Vacuum 169 (2019) 108864, http://dx.doi.org/10.1016/j.vacuum.2019.108864, URL https://www.sciencedirect.com/science/article/pii/S0042207X19312096.

[8] Y. Feng, Z. Zhang, R. Qi, Q. Huang, Z. Wang, Microstructural evolution of Ni/Ti multilayers doped with nitrogen at different d-spacings for neutron supermirrors, Vacuum 210 (2023) 111881, http://dx.doi.org/10.1016/j.vacuum.2023.111881, URL https://www.sciencedirect.com/science/article/pii/S0042207X23000787.

[9] H.M.-L. Zentrum, Neutron Optics Group, 2025, URL https://mlz-garching.de/neutron-optics, (Accessed 15 May 2025).

[10] J.M. Gómez-Guzmán, M. Opel, T. Veres, P. Link, L. Bottyán, Structural, electrical and magnetic properties of reactively dc sputtered cu and ti thin films. Application to Cu/Ti neutron supermirrors for low spin-flip applications, Nucl. Instrum. Methods Phys. Res. Sect. A: Accel. Spectrometers, Detect. Assoc. Equip. 1059 (2024) 169005, http://dx.doi.org/10.1016/j.nima.2023.169005, URL https://www.sciencedirect.com/science/article/pii/S0168900223010057.

[11] Schott, Borofloat®33 Mechanical Properties Datasheet, 2025a, URL https://www.schott.com/en-gb/products/borofloat-p1000314/downloads, (Accessed 15 May 2025).

[12] S. Masalovich, Analysis and design of multilayer structures for neutron monochromators and supermirrors, Nucl. Instrum. Methods Phys. Res. Sect. A: Accel. Spectrometers, Detect. Assoc. Equip. 722 (2013) 71–81, http://dx.doi.org/10.1016/j.nima.2013.04.051, URL https://www.sciencedirect.com/science/article/pii/S0168900213004725.

[13] M.E. Fitzpatrick, A. Fry, P. Holdway, F. Kandil, J. Shackleton, L. Suominen, Determination of Residual Stresses by X-ray Diffraction, National Physical Laboratory, 2005, pp. 89–96.

[14] G. Abadias, E. Chason, J. Keckes, M. Sebastiani, G.B. Thompson, E. Barthel, G.L. Doll, C.E. Murray, C.H. Stoessel, L. Martinu, Review article: Stress in thin films and coatings: Current status, challenges, and prospects, J. Vac. Sci. Technol. A 36 (2) (2018) 020801, http://dx.doi.org/10.1116/1.5011790, arXiv:https://pubs.aip.org/avs/jva/article-pdf/doi/10.1116/1.5011790/19749142/020801_1_online.pdf.

[15] P.S. Prevey, D.J. Hornbach, X-Ray diffraction residual-stress techniques, in: Materials Characterization, ASM International, 2019, http://dx.doi.org/10.31399/asm.hb.v10.a0006632.

[16] R.C. Reed, The Superalloys: Fundamentals and Applications, Cambridge University Press, 2006.

[17] B. Rehmer, F. Bayram, L.A.A. Calderon, G. Mohr, B. Skrotzki, Elastic modulus data for additively and conventionally manufactured variants of Ti-6Al-4V, IN718 and AISI316L, Sci. Data 10:474 (2023) 1–9, http://dx.doi.org/10.1038/s41597-023-02387-6.

[18] J. Everaerts, C. Papadaki, W. Li, A.M. Korsunsky, Evaluation of single crystal elastic stiffness coefficients of a nickel-based superalloy by electron backscatter diffraction and nanoindentation, J. Mech. Phys. Solids 131 (2019) 303–312, http://dx.doi.org/10.1016/j.jmps.2019.07.011, URL https://www.sciencedirect.com/science/article/pii/S0022509619300080.

[19] H. Benzerouk, F. Chouit, M. Mekhnache, L. Saad Hamideche, A. Drici, An experimental and theoretical study of nickel oxide (NiO) using the spraying method (CSP) and DFT calculations, Mater. Sci. Eng.: B 303 (2024) 117323, http://dx.doi.org/10.1016/j.mseb.2024.117323, URL https://www.sciencedirect.com/science/article/pii/S0921510724001521.

[20] Q. Zhang, Z. Zhang, H. Ni, Q. Huang, X. Li, J. He, Z. Wang, Effect of the nitrogen content of sputtering gas during Ni deposition on Ni/Ti periodic multilayers and neutron supermirror performance, J. Appl. Crystallography 56 (3) (2023) 650–659, http://dx.doi.org/10.1107/S1600576723002546.

[21] D. Nečas, P. Klapetek, Gwyddion: an open-source software for SPM data analysis, Central Eur. J. Phys. 10 (2012) 181–188, http://dx.doi.org/10.2478/s11534-011-0096-2.

[22] Paul Scherrer Institute, NARZISS, 2025, URL https://www.psi.ch/de/sinq/narziss, (Accessed 15 May 2025).

[23] Budapest Neutron Center, REF, 2025, URL https://bnc.hu/ref/, (Accessed 15 May 2025).

[24] A. Glavic, M. Björck, *GenX 3*: the latest generation of an established tool, J. Appl. Crystallography 55 (4) (2022) 1063–1071, http://dx.doi.org/10.1107/S1600576722006653.

[25] Schott, 2025b, Email correspondence with Maximilian Enkelmann, Personal communication.

[26] D.R. Lide (Ed.), CRC Handbook of Chemistry and Physics, 86th, CRC Press, Boca Raton, FL, 2005.

[27] P. Villars, Crystallographic data for nickel (Ni), 2024, URL https://springer.com, (Accessed 22 April 2026), SpringerMaterials Database.

[28] J.F. Ziegler, M. Ziegler, J. Biersack, SRIM – the stopping and range of ions in matter (2010), Nucl. Instrum. Methods Phys. Res. Sect. B: Beam Interactions Mater. Atoms 268 (11) (2010) 1818–1823, http://dx.doi.org/10.1016/j.nimb.2010.02.091, URL https://www.sciencedirect.com/science/article/pii/S0168583X10001862, 19th International Conference on Ion Beam Analysis.

[29] T. Gaewdang, N. Wongcharoen, Influence of oxygen flow rate on structural, optical and electrical properties of copper oxide thin films prepared by reactive magnetron sputtering, IOP Conf. Ser.: Mater. Sci. Eng. 211 (1) (2017) 012025, http://dx.doi.org/10.1088/1757-899X/211/1/012025.

[30] V.L. Mironov, O.G. Udalov, B.A. Gribkov, A.A. Fraerman, Comparative x-ray reflectometry and atomic force microscopy of surfaces with non-Gaussian roughness, J. Appl. Phys. 104 (6) (2008) 064301, http://dx.doi.org/10.1063/1.2977753, arXiv:https://pubs.aip.org/aip/jap/article-pdf/doi/10.1063/1.2977753/15025476/064301_1_online.pdf.

[31] H.-C. Su, M.-Z. Lin, T.-W. Huang, C.-H. Lee, Comparison between the atomic force microscopy and x-ray reflectivity on the characterization of the roughness of a surface, in: N. Meyendorf, G.Y. Baaklini, B. Michel (Eds.), Testing, Reliability, and Application of Micro- and Nano-Material Systems II, vol. 5392, International Society for Optics and Photonics, SPIE, 2004, pp. 123–131, http://dx.doi.org/10.1117/12.539761.

[32] Y. Fujii, Comparison of surface roughness estimations by X-ray reflectivity measurements and TEM observations, IOP Conf. Ser.: Mater. Sci. Eng. 24 (1) (2011) 012008, http://dx.doi.org/10.1088/1757-899X/24/1/012008.

[33] O. Filies, O. Böling, K. Grewer, J. Lekki, M. Lekka, Z. Stachura, B. Cleff, Surface roughness of thin layers—a comparison of XRR and SFM measurements, Appl. Surf. Sci. 141 (3) (1999) 357–365, http://dx.doi.org/10.1016/S0169-4332(98)00524-8, URL https://www.sciencedirect.com/science/article/pii/S0169433298005248.

[34] T. Degen, M. Sadki, E. Bron, U. König, G. Nénert, The HighScore suite, Powder Diffr. 29 (S2) (2014) S13–S18, http://dx.doi.org/10.1017/S0885715614000840.

[35] J.I. Langford, A.J.C. Wilson, Scherrer after sixty years: A survey and some new results in the determination of crystallite size, J. Appl. Crystallography 11 (2) (1978) 102–113, http://dx.doi.org/10.1107/S0021889878012844.

[36] I. Bakonyi, V. Isnaini, T. Kolonits, Z. Czigány, J. Gubicza, L. Varga, E. Tóth-Kádár, L. Pogány, L. Péter, H.E. and, The specific grain-boundary electrical resistivity of Ni, Phil. Mag. 99 (9) (2019) 1139–1162, http://dx.doi.org/10.1080/14786435.2019.1580399, arXiv:https://doi.org/10.1080/14786435.2019.1580399.

[37] M.J. Laubitz, T. Matsumura, P.J. Kelly, Transport properties of the ferromagnetic metals. II. Nickel, Can. J. Phys. 54 (1) (1976) 92–102, http://dx.doi.org/10.1139/p76-011, arXiv:https://doi.org/10.1139/p76-011, Quoted as reference data by J. Bass, Chapter 1: Electrical resistivity of pure metals and dilute alloys, in Landolt- Börnstein - Group III, New Series, Springer-Verlag, Berlin, Heidelberg, New York, 1982, Vol. 15a, pp. 1–287.

[38] Q. Luo, A. Jones, High-precision determination of residual stress of polycrystalline coatings using optimised XRD$sin^2\psi$ technique, Surf. Coat. Technol. 205 (5) (2010) 1403–1408, http://dx.doi.org/10.1016/j.surfcoat.2010.07.108, URL https://www.sciencedirect.com/science/article/pii/S0257897210006304, ICMCTF 2010 Special Issue.

[39] R. Schöngrundner, R. Treml, T. Antretter, D. Kozic, W. Ecker, D. Kiener, R. Brunner, Critical assessment of the determination of residual stress profiles in thin films by means of the ion beam layer removal method, Thin Solid Films 564 (2014) 321–330, http://dx.doi.org/10.1016/j.tsf.2014.06.003, URL https://www.sciencedirect.com/science/article/pii/S0040609014006476.

[40] K.J. Martinschitz, E. Eiper, J. Keckes, Stress factors and absolute residual stresses in thin films determined by the combination of curvature and $\sin^2\psi$ methods, in: Residual Stresses VII, ECRS7, in: Materials Science Forum, vol. 524, Trans Tech Publications Ltd, 2006, pp. 711–715, http://dx.doi.org/10.4028/www.scientific.net/MSF.524-525.711.

[41] Q. Luo, S. Yang, Uncertainty of the X-ray diffraction (XRD) $\sin^2\psi$ technique in measuring residual stresses of physical vapor deposition (PVD) hard coatings, Coatings 7 (8) (2017) http://dx.doi.org/10.3390/coatings7080128, URL https://www.mdpi.com/2079-6412/7/8/128.

[42] U. Welzel, J. Ligot, P. Lamparter, A.C. Vermeulen, E.J. Mittemeijer, Stress analysis of polycrystalline thin films and surface regions by X-ray diffraction, J. Appl. Crystallography 38 (1) (2005) 1–29, http://dx.doi.org/10.1107/S0021889804029516.

[43] X. Gao, X. Meng, B. Li, Direct-current-sputtered nickel oxide (NiO) films with improved p-type conduction characteristic: impact of substrate temperature on structure, optical and electrical properties, Phys. Scr. 98 (8) (2023) 085916, http://dx.doi.org/10.1088/1402-4896/ace292.

[44] J.E. Greene, Review article: Tracing the recorded history of thin-film sputter deposition: From the 1800s to 2017, J. Vac. Sci. Technol. A 35 (5) (2017) 05C204, http://dx.doi.org/10.1116/1.4998940, arXiv:https://pubs.aip.org/avs/jva/article-pdf/doi/10.1116/1.4998940/19748996/05c204_1_online.pdf.

[45] M. Senthil Kumar, P. Böni, D. Clemens, Mechanical and structural properties of Ni/Ti multilayers and films: An application to neutron supermirrors, J. Appl. Phys. 84 (12) (1998) 6940–6942, http://dx.doi.org/10.1063/1.368996, arXiv:https://pubs.aip.org/aip/jap/article-pdf/84/12/6940/19120845/6940_1_online.pdf.

[46] K. Holmberg, H. Ronkainen, A. Laukkanen, K. Wallin, S. Hogmark, S. Jacobson, U. Wiklund, R.M. Souza, P. Ståhle, Residual stresses in TiN, DLC and MoS2 coated surfaces with regard to their tribological fracture behaviour, Wear 267 (12) (2009) 2142–2156, http://dx.doi.org/10.1016/j.wear.2009.01.004, URL https://www.sciencedirect.com/science/article/pii/S0043164809000064, NORDTRIB 2008.

[47] B.L. Hackett, A.A. Wereszczak, G.M. Pharr, Effect of aqueous-based mechanical polishing on the nanoindentation response of borosilicate glasses, Int. J. Appl. Glas. Sci. 10 (3) (2019) 302–306, http://dx.doi.org/10.1111/ijag.13108.

[48] V.K. Bajpai, H. Pandey, T. Singh, P. Dixit, Ultrasonic-assisted surface roughening of glass substrate to improve adhesion of electroless nickel seed layer in microsystems packaging, Mater. Lett. 316 (2022) 132033, http://dx.doi.org/10.1016/j.matlet.2022.132033, URL https://www.sciencedirect.com/science/article/pii/S0167577X2200386X.

[49] R. Kolevatov, C. Schanzer, P. Böni, Neutron absorption in supermirror coatings: Effects on shielding, Nucl. Instrum. Methods Phys. Res. Sect. A: Accel. Spectrometers, Detect. Assoc. Equip. 922 (2019) 98–107, http://dx.doi.org/10.1016/j.nima.2018.12.069, URL https://www.sciencedirect.com/science/article/pii/S0168900218318837.

[50] R. Cubitt, G. Fragneto, Chapter 2.8.3 - neutron reflection:: Principles and examples of applications, in: R. Pike, P. Sabatier (Eds.), Scattering, Academic Press, London, 2002, pp. 1198–1208, http://dx.doi.org/10.1016/B978-012613760-6/50065-6, URL https://www.sciencedirect.com/science/article/pii/B9780126137606500656.

[51] T. Krist, A. Teichert, E. Meltchakov, V. Vidal, E. Zoethout, S. Müllender, F. Bijkerk, Stress reduction in multilayers used for X-Ray and neutron optics, in: A. Erko, M. Idir, T. Krist, A.G. Michette (Eds.), Modern Developments in X-Ray and Neutron Optics, Springer Berlin Heidelberg, Berlin, Heidelberg, 2008, pp. 371–388, http://dx.doi.org/10.1007/978-3-540-74561-7_23.

[52] K. Soyama, H. Tsunoda, K. Murakami, Reflectivity enhancement of large m-qc supermirror by ion polishing, Nucl. Instrum. Methods Phys. Res. Sect. A: Accel. Spectrometers, Detect. Assoc. Equip. 529 (1) (2004) 73–77, http://dx.doi.org/10.1016/j.nima.2004.04.180, URL https://www.sciencedirect.com/science/article/pii/S0168900204008629, Proceedings of the Joint Meeting of the International Conference on Neutron Optics (NOP2004) and the Third International Workshop on Position-Sensitive Neutron Detectors (PSND2004).

[53] M. Ay, C. Schanzer, M. Wolff, J. Stahn, New interface solution for Ni/Ti multilayers, Nucl. Instrum. Methods Phys. Res. Sect. A: Accel. Spectrometers, Detect. Assoc. Equip. 562 (1) (2006) 389–392, http://dx.doi.org/10.1016/j.nima.2006.02.188, URL https://www.sciencedirect.com/science/article/pii/S0168900206004785.